Analysis of the Factors that Led to an uncertainty of track forecast of Typhoon Krosa (2019) by 101-member ensemble forecast experiments using NICAM

Masuo NAKANO[1]

*Research Institute for Global Change,
Japan Agency for Marine-Earth Science and Technology (JAMSTEC),
Yokohama, Japan*

Ying-Wen CHEN

*Atmosphere and Ocean Research Institute,
The University of Tokyo, Chiba, Japan*

and

Masaki SATOH

*Atmosphere and Ocean Research Institute,
The University of Tokyo, Chiba, Japan*

April 7, 2022

----

1) Corresponding author: Masuo Nakano, JAMSTEC, 3173-25 Showa-machi, Kanazawa-ku, Yokohama, 236-0001, JAPAN
Email: masuo@jamstec.go.jp
Tel: +81-45-778-5616

Abstract

Typhoon Krosa (2019) formed in the eastern part of the Philippines Sea and ~1400 km east of another typhoon Lekima on August 6th and made a landfall in the western part of Japan's mainland on August 15th. The operational global model forecasts, which were initialized just after Krosa's formation, showed a very large uncertainty and totally failed to predict the actual track of Krosa. In this study, we investigated the causes of this large uncertainty through 101-member ensemble forecast experiments by using a 28-km mesh global nonhydrostatic model. The experiments initialized at 12 UTC, August 6th, showed a large uncertainty. An ensemble-based sensitivity analysis indicated that the western North Pacific Subtropical High (WNPSH) retreated further east in the members with large track forecast errors than in the members with small errors. The members with a large track forecast error for Krosa, Krosa and Lekima approached by 250 km and Krosa propagated northward faster than the observation in 36 hours from the initialization time. For the members with a small track forecast error for Krosa, two typhoons approached by only 50 km, and the northward propagation speed was comparable with that of the observation. The typhoon relative composite analysis exhibited that at the initialization time, the members with a large Krosa track forecast error had a larger horizontal size of Krosa and higher moisture in the east of Krosa's center. The difference in Krosa's size was kept during the forecast period, and precipitation was larger in the outer region for the members with a large Krosa's track error. This difference led to a stronger interaction between the two typhoons, thus resulting in a fast

northward propagation speed for the members with a large Krosa track error.

Keywords tropical cyclone; track forecast; Fujiwhara effect; forecast bust; western North Pacific subtropical high

1. Introduction

Tropical cyclones (TCs) often cause destructive disasters and threaten human lives and socioeconomies. To mitigate the damages caused by TCs, continuous efforts are needed to improve track forecasts. By 2030, the Japan Meteorological Agency (JMA) aims at reducing the track forecast errors of typhoons on day 3 to less than 100 km, which is approximately half the current forecast error (see Fig 4.1 of JMA 2020). The forecasting of TC tracks has significantly been improved in recent decades. However, the forecasts occasionally experience unusual large errors or uncertainties, which are sometimes called “forecast busts.” Thus, to further improve the track forecasts of TCs, it is necessary to understand what causes such unusual large forecast errors or uncertainties.

Typhoon Krosa (2019) took place at 06 UTC, August 6th, in the eastern part of the Philippines Sea under the convective envelope associated with the boreal summer intraseasonal oscillation (BSISO; Wang and Rui 1990; Wang and Xie 1997; Kikuchi 2021). Afterward, by August 8th, it propagated northwestward, and by August 11th, it slowed down and made a complex trajectory. Subsequently, on August 15th, it propagated northwest/north-northwest again and made a landfall on the Hiroshima prefecture, the western part of the mainland of Japan. It should be noted that at the formation time of Krosa, another typhoon, Lekima, was located at ~1400 km west of Krosa. Lekima propagated northwestward and made a landfall on the central part of the mainland of China on August 9th.

The operational models initialized at 12 UTC, August 6th, showed a very large uncertainty in forecasting Krosa’s track (Fig. 1). For example, the European

Fig. 1

Center for Medium-Range Weather Forecasts (ECMWF) and JMA models barely captured the observed Krosa's track within the uncertainty range. However, the spread was very high; the westernmost track would hit Korea, and the easternmost track would go through the oceanic area east of Japan without making a landfall. The National Centers for Environmental Prediction (NCEP) model showed a small uncertainty; however, it totally failed to predict the actual track of Krosa; all members predicted that Krosa would go through to the east of Japan without making a landfall. For the later model initialization time, the uncertainty of Krosa's track forecast decreased, and the forecasts of the three models were converged to the observed track at 12 UTC, August 9th.

In the western North Pacific (WNP) region, it is well known that the WNP subtropical high (WNPSH) strongly modulates TC tracks in various time scales. TC tracks are modulated by the convective activity in the tropics since it affects the westward extension of WNPSH (Lu and Dong 2001). Nakazawa and Rajendran (2007) found that the seasonal number of TCs approaching Japan or making a landfall on it is strongly modulated by the presence of an anticyclonic anomalous circulation east of the Philippines due to the shifting of the WNPSH westward, resulting in a lower-than-normal TC frequency over Japan. Choi et al. (2010) showed that the Pacific–Japan pattern (Nitta 1987) changes the TC activity in WNP. In addition, Nakano et al. (2021) showed that the suppressed and enhanced convection associated with BSISO affects TC tracks, and this impact is well reproduced by the ECMWF model. Camp et al. (2019) showed the potential of TC landfall seasonal forecasts by using WNPSH indices predicted by UK MetOffice's global seasonal forecast system in June–August. It is worth noting that a TC creates anticyclonic anomaly northeast of its location due to the Rossby response to its convective heating (Kawamura and Ogasawara 2006), resulting in WNPSH enhancement.

In the cases when two or more TCs closely coexist, they interact with each other (a.k.a. “Fujiwhara effect”; Fujiwhara 1921, 1923). Brand (1970) showed that the interaction characteristics depend on the separation distance between such TCs; rotating cyclonically within each other when the separation distance is less than 750 NM (~1390 km) and attracting each other when the separation distance is less than 400 NM (~740 km). Peng (2005) showed that an interaction can occur even when the distance is 1861 km. Moreover, Brand (1970) mentioned that the track forecast errors for TCs the Fujiwhara effect taking in place were larger than average in the 1960’s. The forecast bust cases associated with such storms can still be seen in state-of-the-art numerical weather prediction systems (e.g., Choi et al. 2017).

The ensemble-based sensitivity analysis (Ancell and Hakim 2007; Torn and Hakim 2008) and clustering the ensemble members by using a ranking of a metric or the characteristics of predicted TC tracks are used to diagnose the main cause of forecast bust. Nakashita and Enomoto (2021) performed an ensemble sensitivity analysis for Typhoon Hagibis (2019) and found that the ensemble members with large track errors have an initial perturbation to weaken the ridge of WNPSH. Magnusson et al. (2014) explored the main causes of the uncertainties in the forecasting of Hurricane Sandy (2012), which made a landfall on the eastern coast of the US from the Atlantic, by grouping the ensemble members into landfall members and moving to the eastern members.

In this study, we investigated the main causes of the large uncertainty in

Krosa's track forecasting through 101-member ensemble forecast experiments by using a global nonhydrostatic model. The rest of this paper is organized as follows. Section 2 describes the experimental setup of the ensemble forecast experiments. Section 3 introduces the data utilized in this study except for the model experimental data and explains the analysis methods. Section 4 shows the results of the experiments, a discussion, and a comparison of the operational model data. Section 5 presents the summary and conclusions of this study.

2. Model Experiment

The model used in this study is a 28-km mesh Nonhydrostatic ICosahedral Atmospheric Model (NICAM [version NICAM.18]; Satoh et al. 2014; Kodama et al. 2021). The number of vertical layers was set to 38, and the model top was located at 37 km. The moist convection was explicitly calculated using a single-moment cloud microphysics scheme (Roh and Satoh 2014) without any cumulus parameterization. The atmospheric initial condition was provided by an operational weather analysis system called NICAM-LETKF JAXA Research Analysis (NEXRA, https://www.eorc.jaxa.jp/theme/NEXRA/index_e.htm, Kotsuki et al. 2019). NEXRA's core data assimilation system is NICAM-LETKF (Terasaki and Miyoshi 2017; Kotsuki et al. 2017), and it combines the ensemble simulation obtained by NICAM and the in situ/satellite observations by LETKF (local ensemble transformed Kalman filter, Hunt et al. 2017). Note that the ensemble size and horizontal resolution of NEXRA were 100 and 112 km, respectively. We used all the ensemble analysis members (100) and their mean for the model initialization. Thus, there were 101 members in total. SST was predicted by a slab ocean model with a constant depth of 15 m. Moreover, SST was nudged toward the initial values with an e-folding time of 7 days. The initial value of SST (1°×1° horizontal resolution) was obtained from the Global Data Assimilation System of NCEP. The SST data was also used in NEXRA's data assimilation cycle. The model simulations were initialized at 12:00 UTC from the 6^{th} to the 9^{th} of August and integrated for 10 days to examine whether the model can reproduce a large uncertainty.

3. Data and Method

The best track data of the Regional Specialized Meteorological Center (RSMC; Tokyo) was used as observational data of the TC location and minimum sea level pressure (SLP). The operational ensemble forecasts of ECMWF, JMA, and NCEP (see Table 1), which were taken from the International Grand Global Ensemble archive (TIGGE; Bougeault et al. 2010; Swinbank et al. 2016), were used for the comparison with the NICAM forecasts and discussion. As the resolution of archived data varies by the operational center and is the coarsest for JMA data, the other center's data was regridded to the same resolution, 1.25 × 1.25 deg.

Table 1

As analyzed by Nakano et al. (2017), the TCs in the model were tracked by searching the SLP minimum nearest to the observed TC center at the initial time and by connecting the nearest SLP minimum along with the forecast period. Before searching the SLP minimum, the SLP field was smoothed 100 times using a Gaussian (1-2-1) filter to avoid tracking a spurious minimum, which can be caused by numerical noise (e.g., so-called grid storm). To define the TC center in NEXRA, the geopotential height at 925 hPa was used instead of the SLP because the SLP for each ensemble member was not available.

To examine the sensitivity of Krosa's track forecast, we performed a lagged correlation analysis and a best-worst comparison. In the former analysis, the correlation between the track forecast errors at a specific time and the atmospheric fields (e.g., geopotential height at 500 hPa) at any forecast lead time and spatial grid were calculated using the simulated data of each ensemble member. In the latter analysis, the best 20% and worst 20% ensemble members in terms of the TC track forecast errors for Krosa were selected. Then, the difference in the ensemble mean of each group was analyzed.

4. Results and Discussion

4.1 General results

Figure 2 shows the predicted Krosa's track in all the ensemble simulations by NICAM. The simulations initialized at 12:00 UTC, August 6th represent a large uncertainty in Krosa's track; the westernmost track makes a landfall on the Korean Peninsula, and the easternmost track passes through the east of the Japanese Island without making a landfall. The uncertainty decreases with a later model initialization date with a slight eastward bias. The simulations initialized at 00:00 UTC, August 9th reasonably capture the observed Krosa's track. This uncertainty reduction in the latter model initialization date was also seen in the operational ensemble forecast system. Thus, the main uncertainty

Fig. 2

cause can be analyzed in detail using the NICAM simulation data initialized at 12:00 UTC, August 6th.

TC tracks are generally affected by vertically averaged flows, which are also called steering flows. If the atmosphere has an equivalent barotropic structure, the steering flow can be roughly represented as a geostrophic flow at 500 hPa. Therefore, the ensemble-based sensitivity analysis was performed using the geopotential height at 500 hPa (Z500) and Krosa's track forecast error at 12:00 UTC, August 11th (Fig. 3). There was no high sensitivity region in NEXRA, which was used to initialize the model at the model initialization time. At the forecast time of 12 hours (FT = 12 h), the correlation between Z500 and Krosa's track forecast error on August 11th became low between the two typhoons of Krosa and Lekima, and the region extended toward the Japanese Island along with the forecast time. This result indicates that Z500 is relatively low (high) in the member with a large (small) Krosa track forecast error. In addition to the negative correlation region, two positive correlation regions appeared in the northwest of Lekima's center and southeast of Krosa's center. This indicates that Z500 is relatively high (low) in the members with large (small) track forecast errors for Krosa. These results suggest that Krosa's track forecast is sensitive to the distance between the two typhoons.

Fig. 3

To examine the mechanism behind this forecast sensitivity, the best 20% and worst 20% members (20 members for both) in terms of Krosa's track forecast errors on August 11th were selected and compared with each other. The best (worst) members had a forecast track error of less than 600 km (more than 1700 km) on August 11th. Figure 4 represents Krosa and Lekima's track forecasts for the best, worst, and other members. The best members predicted

Fig. 4

a stall in Krosa from the 9th to the 11th of August and subsequent northwestward or north-northwestward track. The other members predicted a fast northward propagation of Krosa two days after the model initialization time and that the typhoon would move toward the east of Japan. For Lekima's track forecast, the best members well captured the observed track. However, the other members predicted the recurvature of Lekima toward Japan. Also, the large error members (worst members) predicted a fast northeastward propagation of Lekima. These results suggest that the main cause of the track forecast errors of both typhoons is the same.

Figure 5 shows that 5860-m (approximating the edge of WNPSH) and 5760-m (indicating Krosa and Lekima) contours simulated by the best and worst members. Although there was a little difference between the ensemble means of the best and worst members at FT=12 h, the differences became apparent afterward. With the worst members, Krosa predicted northwest of the Krosa predicted with the best members. However, the difference for Lekima was little. Thus, the distance between the two typhoons was small with the worst members. In addition, the WNPSH over Japan retreated further east with the worst members. These features can also be seen in FT = 36 h. These results are consistent with those of the ensemble-based sensitivity analysis (Fig. 3). Fig. 5

Figure 6 shows the ensemble mean of six-hourly positions of the two typhoons predicted with the best and worst members. Whereas Krosa propagated northward fast with the worst members, the northward migration with the best members was slow and was almost stalled after FT=48 h. With the best members, Lekima propagated northwestward faster than with the worst members. In addition, with the worst members, the curvature of Lekima was Fig. 6

predicted at approximately FT = 48 h. Krosa's track forecast error with the worst members rapidly grew after FT = 18 h and become greater than 1000 km at FT = 66. However, Krosa's track forecast error was not so large (~220 km) with the best members at FT = 72. It is worth noting that the position error at FT = 1 h is slightly larger with the worst members than with the best members. Lekima's track forecast error was almost the same among the best and worst members at FT = 6 h. However, the error with the worst members became greater in the latter forecast time and rapidly grew starting from FT = 48 h. The distance between the two typhoons with the worst members was 1400 km at FT = 1 h. Afterward, it decreased to 1150 km by FT = 36 h and then increased at the later forecast time. The best members had little distance changes at FT = 24 h. However, the distance rapidly increased at a later forecast time. Assuming that both groups represent the same vortex structure of the typhoons, the interaction between both typhoons could occur easily when the distance between the two typhoons was close. Thus, the interaction between the two typhoons would be stronger with the worst members than with the best members. The predicted Krosa's central minimum pressure is deeper than the best track data from the initial time to FT = 30 h with both members. The model represented Lekima to be shallower in both members than analyzed with the best track. Thus, the bias in the central pressure for both typhoons seems not to be related to the track forecast error.

These results suggest that the retreatment of WNPSH and the degree of interaction between the two typhoons affected the uncertainty of Krosa's track forecast. These two points are discussed in the following subsections.

4.1.1 Why did a difference in WNPSH occur?

Generally, the intensity of WNPSH is affected by the convective activity near the Philippines. In the present case, Krosa and Lekima existed side by side in the east and west. Therefore, the convective activities of the two typhoons would affect WNPSH. Figure 7 shows the ensemble mean of the geopotential height and the divergence of the horizontal wind for the best and worst members at 150 hPa and 925 hPa (averaged from FT = 6 h to FT = 36 h). A tripolar structure can be seen with both members at 150 hPa; the divergence aloft each typhoon and the convergence near 30°N 140–145°E existed. In the difference between the ensemble means of the best and worst members, weak low-pressure anomaly with eastward tilt and corresponding convergence anomaly along with 140°E existed. To the southeast of the anomalies, slightly high-presssure and divergent anomalies can be seen. At 925 hPa, there are two convergence areas corresponding to the inflow of the typhoons and the weak divergence area near 30°N. In the difference between the best and worst members, there are divergence and anticyclone anomalies corresponding to the convergence and cyclonic anomalies at 150 hPa. Also, to the southeast of the anomalies, there are convergence and anticyclonic anomalies corresponding to the divergent and anticyclonic anomalies at 150hPa. These dipole anomaly structures in the tropopause and near the surface were induced by differences in Krosa's location between the best and worst members. It is worth noting that this anticyclonic anomaly at 925 hPa corresponds well to the region with a negative correlation in the ensemble-based sensitivity analysis. Thus, the difference in Krosa's location between the best and worst members caused anomalies of mass concentration through the convergence anomalies near the tropopause, leading to a difference in the

Fig. 7

westward extension of WNPSH.

4.2 Why did the strong interaction occur in the worst members?

Fig. 8

Figure 8 shows the locations of the typhoons' centers for both the best and worst members and the ensemble mean SLP distributions. The existence frequency of the typhoons' centers in the east-west and south-north directions are also shown. At FT = 1 h, Krosa's SLP distributions for the worst members slightly shifted to the west toward the distributions of the best members. Corresponding to this westward shift, the existence frequency of Krosa's center in the east of 142°E was less with the worst members than with the best members, whereas the frequency was almost the same in the south-north direction for both members. At FT = 12 h, the SLP distributions of Krosa with the worst members shifted to the northwest of those with the best members. The analyzed center location was well captured by the simulated existence frequency with the best members. However, it is out of range of the simulated existence frequency by the worst member, especially in the east-west direction. Nevertheless, the SLP distribution and existence frequency of the typhoon center for Lekima were almost the same with both the best and worst members.

Fig. 9

To examine the differences in the typhoon structure, a composite analysis relative to the typhoon's center was performed. Figure 9 shows the composite around Krosa's center in NEXRA at the model initialization time. The low area near the western edge represents Lekima. The 680-m contour was separated in the composite of the best member; however, it was connected to Lekima in the composite of the worst members. The differences in Z925 indicate that there was an anticyclonic anomaly north and northwest of Krosa's center with the best members in comparison with the worst members. The 10-m wind speed was larger at the east of Krosa's center with both the best and worst members than at the west. The small wind speed was induced by a confluence of the northerly wind by Krosa and the southerly wind by Lekima. The difference between the best and worst members indicates the weak wind speed anomaly in the eastern semicircle. The specific humidity was high near Krosa's center and to the west of it. The difference between the best and worst members shows that there was a dry anomaly at the eastern side of Krosa (by 0.5 g/kg).

Although apparent differences in the vortex structure of Krosa could be found between the best and worst members, a very little difference in Lekima's structure was found (Fig.10). Z925 was slightly higher with the best members than with the worst members. However, the higher Z925 area was limited around Lekima's center. Corresponding to the Z925 anomaly, low wind speed anomalies could be observed in the northern and western sides, which are very close to Lekima's center. The anomaly of 10 degrees east of Lekima's center can be related to the differences in Krosa's position and size. Thus, the confluence region of Krosa's northerly and Lekima's southerly regions was shifted to the west more with the worst members than with the best members. Fig. 10

Figure 11a shows the SLP and precipitation amount averaged over FT = 1–12 h around Krosa. The 1000 hPa SLP contour was connected with both the best and worst members. However, it was more open with the worst members. Heavy precipitation occurred at the south of Krosa with both members. The difference shows that more intense precipitation occurred at the southeast quadrant with the best members than with the worst members. The worst members had more precipitation at the southwest of Krosa's center and eastern part of the outer core region. Figure 11b shows the 10 m wind averaged over FT Fig. 11

= 1–12 h around Krosa. The 10-m wind speed of the inner core region with the best members was higher than that with the worst members; however, the wind speed was higher 5 degrees east of Krosa with the worst members. These results show that the best members led to smaller and more intense vortex structures than the worst members. With the worst members, more intense convection occurred in the outer area than with the best members. Therefore, the vortex could not shrink and would not become intense. These results suggest that Krosa's structure at the initial condition affected the vortex structure in the model forecast. The initial vortex structure, which was larger in size and wetter in the outer region with the worst members, led to convection in the outer region. Thus, the larger vortex structure and stronger interaction with Lekima with the worst members were withheld.

4.3 Did the same situation happen in the operational models?

The readers may wonder whether the proposed mechanism worked in the operational ensemble forecast systems. The operational centers' forecasts were grouped into best and worst and then compared to speculate this point. However, analyzing the mechanism in detail using operational model data is beyond the aim of this paper, as the archived data resolution is coarser than the actual model resolution. Figure 12 shows the spaghetti diagram of Z500 for the best and worst members for each operational system initialized at 12 UTC, August 6th. There is no obvious difference at 00:00 UTC, August 8th, whereas NICAM showed apparent differences (Fig. 5). However, by August 10th, WNPSH retreated more eastward with the worst members than with the best members. In addition, Krosa's northward propagation was faster at all centers, and Lekima's northward propagation was slower at all centers with the worst

Fig. 12

members except for JMA. Thus, with the worst members, Krosa and Lekima would rotate around each other in an anticlockwise direction. Overall, these results suggest that, as found in the NICAM simulations, the interaction between Krosa and Lekima would occur stronger with the worst members than with the best members and that it is associated with the eastward retreat of WNPSH.

5. Summary and Conclusion

In this study, the main cause of the uncertainty in forecasting Krosa's track, as seen in the operational ensemble forecast data, was examined by a 101-member ensemble forecast by NICAM, which was initialized using the LETKF-based data assimilation product NEXRA. The large uncertainty in the model initialized at 12:00 UTC, August 6th and the decrease in uncertainty as the model initialization time went by, as predicted by the operational systems, were successfully reproduced by NICAM. The ensemble-based sensitivity analysis of Krosa's track forecast error suggested that the track error was sensitive to the intensity of WNPSH over Japan and the distance between Krosa and Lekima. The best and worst members (20 for each) in terms of Krosa's forecast track error were compared. The westward extension of WNPSH was stronger with the best members, and the northward propagation of Krosa was faster with the worst members. The distance between Krosa and Lekima decreased by 250 km in 36 hours after the model initialization time with the worst members, whereas the distance was almost constant in 24 hours after the model initialization time with the best members. These results suggest that a strong interaction between Krosa and Lekima occurred with the worst members, leading to a fast northward propagation and a large track forecast error.

The difference in the composite fields between the best and worst members indicates that Krosa had a larger vortex size and was wetter in the eastern side of the vortex center with the worst members than with the best members at the initial conditions. However, little differences were found around Lekima. These differences led to more precipitation in the outer area of Krosa, resulting in its larger vortex size with the worst members of the NICAM forecasts. The convergence difference near the tropopause level and the divergence near the surface were caused by the difference in Krosa's location. These results suggest that the analysis error around Krosa in NEXRA, which was used in the NICAM forecasts, determines whether a strong interaction between Krosa and Lekima would occur or not. This strong interaction resulted in the retreat of WNPSH. The analysis of the operational models suggests that the same mechanism also worked in these models whereas the timing is later than NICAM.

Considering that BSISO sometimes causes multiple TC formations, such as in the present case, examining whether the track forecast busts associated with BSISO occur or not is the next step to further improve TC forecasting. Lekima and Krosa were formed under a convective envelope associated with BSISO. There is a possibility that it was difficult to obtain enough observational data to constrain the model, especially at the initial phase of Krosa. Recent studies have shown that assimilating all-sky radiance data improves TC forecasting (Honda et al. 2018; Minamide and Zhang 2018). Thus, implementing such advanced methods to NEXRA and quantifying the improvement rate of TC forecasting under many cases would be useful future works (e.g., Nakano et al.

2017).

Data Availability Statement

The NEXRA analysis data are available upon request to the NEXRA development team (Z-NEXRA_ADMIN@ml.jaxa.jp). All the data from ensemble experiments by NICAM will be provided from M.N. upon request.

Supplement

None

Declaration

The authors have no conflicts of interest to declare.

Author contributions

M.N designed and conducted the experiments and wrote the manuscript. W.-Y. C. and M.S. discussed about results with M.N. and edited and approved the manuscript.

Acknowledgments

This work was supported by MEXT (JPMXP1020351142) as “Program for Promoting Researches on the Supercomputer Fugaku” (Large Ensemble Atmospheric and Environmental Prediction for Disaster Prevention and

Mitigation) and KAKENHI (JP20H05728 and JP20H05730). All the simulation was performed on the Earth Simulator (NEC SX-ACE) of JAMSTEC and the simulation data was post-processed on the data analyzer of JAMSTEC. The TIGGE data was obtained from MARS system of ECMWF. The ensemble analysis data obtained from NEXRA are produced on the second generation JAXA's supercomputer system (JSS2). The TC tracking tool was provided by Dr. M. Sawada of JMA.

References

Ancell, B., and G. J. Hakim, 2007: Comparing Adjoint- and Ensemble-Sensitivity Analysis with Applications to Observation Targeting. *Mon. Weather Rev.*, **135**, 4117–4134, https://doi.org/10.1175/2007MWR1904.1.

Bougeault, P., and Coauthors, 2010: The THORPEX Interactive Grand Global Ensemble. *Bull. Am. Meteorol. Soc.*, **91**, 1059–1072, https://doi.org/10.1175/2010BAMS2853.1.

Brand, S., 1970: Interaction of Binary Tropical Cyclones of the Western North Pacific Ocean. *J. Appl. Meteorol. Climatol.*, **9**, 433–441, https://doi.org/10.1175/1520-0450(1970)009<0433:IOBTCO>2.0.CO;2.

Camp, J., and Coauthors, 2019: The western Pacific subtropical high and tropical cyclone landfall: Seasonal forecasts using the Met Office GloSea5 system. *Quart. J. Roy. Meteor. Soc.*, **145**, 105–116, https://doi.org/10.1002/qj.3407.

Choi, K.-S., C.-C. Wu, and E.-J. Cha, 2010: Change of tropical cyclone activity by Pacific-Japan teleconnection pattern in the western North Pacific. *J. Geophys. Res.*, **115**, https://doi.org/10.1029/2010jd013866.

Choi, Y., D.-H. Cha, M.-I. Lee, J. Kim, C.-S. Jin, S.-H. Park, and M.-S. Joh, 2017: Satellite radiance data assimilation for binary tropical cyclone cases over the western N orth P acific. *J. Adv. Model. Earth Syst.*, **9**, 832–853, https://doi.org/10.1002/2016ms000826.

Fujiwhara, S., 1921: The natural tendency towards symmetry of motion and its application as a principle in meteorology. *Quart. J. Roy. Meteor. Soc.*, **47**, 287–292, https://doi.org/10.1002/qj.49704720010.

——, 1923: On the growth and decay of vortical systems. *Quart. J. Roy. Meteor. Soc.*, **49**, 75–104, https://doi.org/10.1002/qj.49704920602.

Honda, T., and Coauthors, 2018: Assimilating All-Sky Himawari-8 Satellite Infrared Radiances: A Case of Typhoon Soudelor (2015). *Mon. Weather Rev.*, **146**, 213–229, https://doi.org/10.1175/MWR-D-16-0357.1.

Hunt, B. R., E. J. Kostelich, and I. Szunyogh, 2007: Efficient data assimilation for spatiotemporal chaos: A local ensemble transform Kalman filter. *Physica D*, **230**, 112–126, https://doi.org/10.1016/j.physd.2006.11.008.

Japan Meteorological Agency, 2020: *Annual Report on the Activities of the RSMC Tokyo - Typhoon Center 2019*. 115 pp. https://www.jma.go.jp/jma/jma-eng/jma-center/rsmc-hp-pub-eg/AnnualReport/2019/Text/Text2019.pdf.

Kawamura, R., and T. Ogasawara, 2006: On the Role of Typhoons in Generating PJ Teleconnection Patterns over the Western North Pacific in Late Summer. *SOLA*, **2**, 37–40, https://doi.org/10.2151/sola.2006-010.

Kikuchi, K., 2021: The Boreal Summer Intraseasonal Oscillation (BSISO): A Review. *Journal of Meteorological Society of Japan*, **advpub**, https://doi.org/10.2151/jmsj.2021-045.

Kodama, C., and Coauthors, 2021: The Nonhydrostatic ICosahedral Atmospheric Model for CMIP6 HighResMIP simulations (NICAM16-S): experimental design, model description, and impacts of model updates. *Geoscientific Model Development*, **14**, 795–820, https://doi.org/10.5194/gmd-14-795-2021.

Kotsuki, S., K. Terasaki, K. Kanemaru, M. Satoh, T. Kubota, and T. Miyoshi, 2019: Predictability of record-breaking rainfall in Japan in july 2018: Ensemble forecast experiments with the near-real-time global atmospheric data assimilation system NEXRA. *Scientific Online Letters on the Atmosphere*, **15**, 1–7, https://doi.org/10.2151/SOLA.15A-001.

Lu, R., and B. Dong, 2001: Westward Extension of North Pacific Subtropical High in Summer. *Journal of the Meteorological Society of Japan*, **79**, 1229–1241, https://doi.org/10.2151/jmsj.79.1229.

Magnusson, L., J.-R. Bidlot, S. T. K. Lang, A. Thorpe, N. Wedi, and M. Yamaguchi, 2014: Evaluation of Medium-Range Forecasts for Hurricane Sandy. *Mon. Weather Rev.*, **142**, 1962–1981, https://doi.org/10.1175/MWR-D-13-00228.1.

Minamide, M., and F. Zhang, 2018: Assimilation of All-Sky Infrared Radiances from Himawari-8 and Impacts of Moisture and Hydrometer Initialization on Convection-Permitting Tropical Cyclone Prediction. *Mon. Weather Rev.*, **146**, 3241–3258, https://doi.org/10.1175/MWR-D-17-0367.1.

Nakano, M., and Coauthors, 2017: Global 7 km mesh nonhydrostatic Model Intercomparison Project for improving TYphoon forecast (TYMIP-G7): experimental design and preliminary results. *Geoscientific Model Development*, **10**, 1363–1381, https://doi.org/10.5194/gmd-10-1363-2017.

Nakano, M., F. Vitart, and K. Kikuchi, 2021: Impact of the boreal summer intraseasonal oscillation on typhoon tracks in the western north pacific and the prediction skill of the ECMWF model. *Geophys. Res. Lett.*, **48**, https://doi.org/10.1029/2020gl091505.

Nakashita, S., and T. Enomoto, 2021: Factors for an Abrupt Increase in Track Forecast Error of Typhoon Hagibis (2019). *SOLA*, **advpub**, https://doi.org/10.2151/sola.17A-006.

Nakazawa, T., and K. Rajendran, 2007: Relationship between Tropospheric Circulation over the Western North Pacific and Tropical Cyclone Approach/Landfall on Japan. *J. Meteorol. Soc. Japan*, **85**, 101–114, https://doi.org/10.2151/jmsj.85.101.

Nitta, T., 1987: Convective activities in the tropical western Pacific and their impact on the Northern Hemisphere summer circulation. *J. Meteorol. Soc. Japan*, **65**, 373–390.

Peng, M. S., 2005: Double trouble for typhoon forecasters. *Geophys. Res. Lett.*, **32**, https://doi.org/10.1029/2004gl021680.

Roh, W., and M. Satoh, 2014: Evaluation of Precipitating Hydrometeor Parameterizations in a Single-Moment Bulk Microphysics Scheme for Deep Convective Systems over the Tropical Central Pacific. *J. Atmos. Sci.*, **71**, 2654–2673, https://doi.org/10.1175/JAS-D-13-0252.1.

Satoh, M., and Coauthors, 2014: The Non-hydrostatic Icosahedral Atmospheric Model: description and development. *Progress in Earth and Planetary Science*, **1**, 1–32, https://doi.org/10.1186/s40645-014-0018-1.

Swinbank, R., and Coauthors, 2016: The TIGGE Project and Its Achievements. *Bull. Am. Meteorol. Soc.*, **97**, 49–67, https://doi.org/10.1175/BAMS-D-13-00191.1.

Torn, R. D., and G. J. Hakim, 2008: Ensemble-Based Sensitivity Analysis. *Mon. Weather Rev.*, **136**, 663–677, https://doi.org/10.1175/2007MWR2132.1.

Wang, B., and H. Rui, 1990: Synoptic climatology of transient tropical intraseasonal convection anomalies: 1975-1985. *Meteorol. Atmos. Phys.*, **44**, 43–61, https://doi.org/10.1007/BF01026810.

Wang, B., and X. Xie, 1997: A model for the boreal summer intraseasonal oscillation. *J. Atmos. Sci.*, **54**, 72–86, https://doi.org/10.1175/1520-0469(1997)054<0072:AMFTBS>2.0.CO;2.

List of Figures

Fig. 1. Track forecast for Krosa (2019) by the ECMWF (a-d), JMA(e-h), and NCEP (i-l) models, initialized at 12:00 UTC, August 6th (a, e, i); 12: 00 UTC, August 7th (b, f, j); 12:00 UTC, August 8th (c, g, k); and 12:00 UTC, August 9th (d, h, l), respectively.

Fig. 2. Track forest for Krosa (a–d) and Lekima (e–h) by NICAM, initialized at 12:00 UTC, August 6th (a, e); 12:00 UTC, August 7th (b, f); 12:00 UTC, August 8th (c, g); and 12:00 UTC, August 9th (d, h), respectively.

Fig. 3. Ensemble lag correlation between the 500-hPa geopotential height for 12:00 UTC, August 6th (a); 00:00 UTC, August 7th (b); 12:00 UTC, August 6th (c); and 00:00 UTC, August 7th (d) and Krosa's track forecast error at 12:00 UTC, August 11th.

Fig. 4. Clustered track forecast for Krosa (a–c) and Lekima (d–f), initialized at 12:00 UTC, August 6th by the track forecast error for Krosa at 12:00 UTC, August 11th. Best 20 members (a and d), worst 20 members (c and f), and the remaining members (b and e).

Fig. 5. Spaghetti diagram of the 500-hPa geopotential height valid for (a) 00:00 UTC, August 7th; (b) 12:00 UTC, August 7th; and (c) 00:00 UTC, August 8th. The orange (aqua) contours are forecasted by the worst (best) 20 members, and the thick lines are ensemble means of the best and worst members. The contours

for 5760 and 5860 m are shown.

Fig. 6. Ensemble means of the best (blue) and worst members (red). (a) Track forecast, (b) track forecast error, (c) distance between Lekima and Krosa, and (d) central sea level pressure. The plus (+) symbol is for Lekima, and the cross (x) symbol is for Krosa.

Fig. 7. Composite of the geopotential height and the divergences at 150 hPa (a–b) and 925 hPa (d–e), simulated for the best (a, d) and worst (b, e) 20 members and their differences (c, f).

Fig. 8. Distributions of the TC center position and sea level pressure at FT = 1 (a, c) and FT = 12 (b, d) for Krosa (a–b) and Lekima (c–d).

Fig. 9. Ensemble means of (a-b) SLP, (d-e) 10-m wind, and (g-h) specific humidity at 925 hPa, analyzed for the best (a,d,g) and worst (b, e, h) 20 members at 12:00 UTC, August 6th and their differences (c, f, i) around Krosa.

Fig. 10. Same as Fig. 9 but for around Lekima.

Fig. 11. TC relative composite of (a-b) SLP and precipitation and (d-e) 10-m wind during FT = 1–12 hours simulated for the best (a, d) and worst (b, e) members and their differences (c, f).

Fig. 12. Spaghetti diagram of the 500-hPa geopotential height valid for (a, d, g)

00:00 UTC, August 8th; (b, e, h) 00:00 UTC, August 9th; and (c, f, i) 00:00 UTC, August 10th by the ECMWF (a-c), JMA (d-f), and NCEP (g-i) models, initialized at 12:00 UTC, August 6th. The thin orange (aqua) contours were forecasted by the worst (best) 20% (10 for ECMWF, 5 for JMA, 4 for NCEP) of the members in terms of the Krosa track forecast error at 12:00 UTC, August 11th. The thick lines are ensemble means of the best and worst members, respectively. The black contours show the analysis by each model. The contours for 5760 and 5860 m are shown.

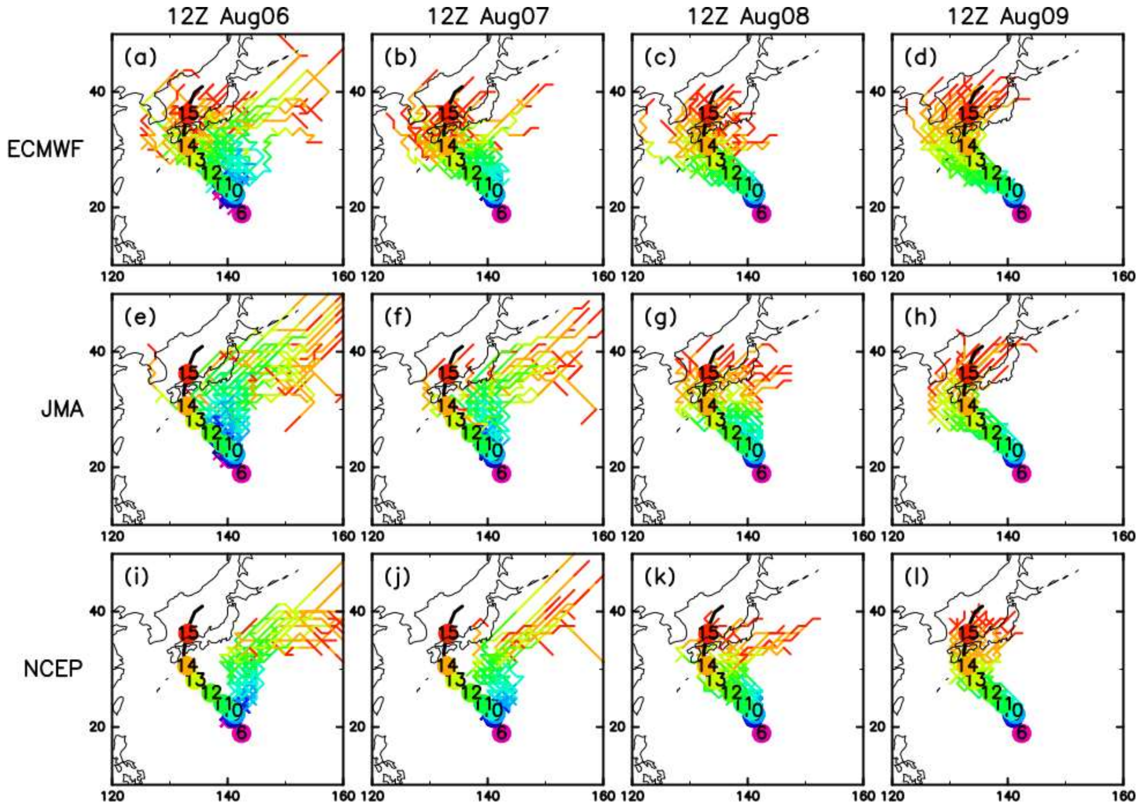

Fig. 1 Track forecast for Krosa (2019) by the ECMWF (a-d), JMA(e-h), and NCEP (i-l) models, initialized at 12:00 UTC, August 6^{th} (a, e, i); 12: 00 UTC, August 7^{th} (b, f, j); 12:00 UTC, August 8^{th} (c, g, k); and 12:00 UTC, August 9^{th} (d, h, l), respectively.

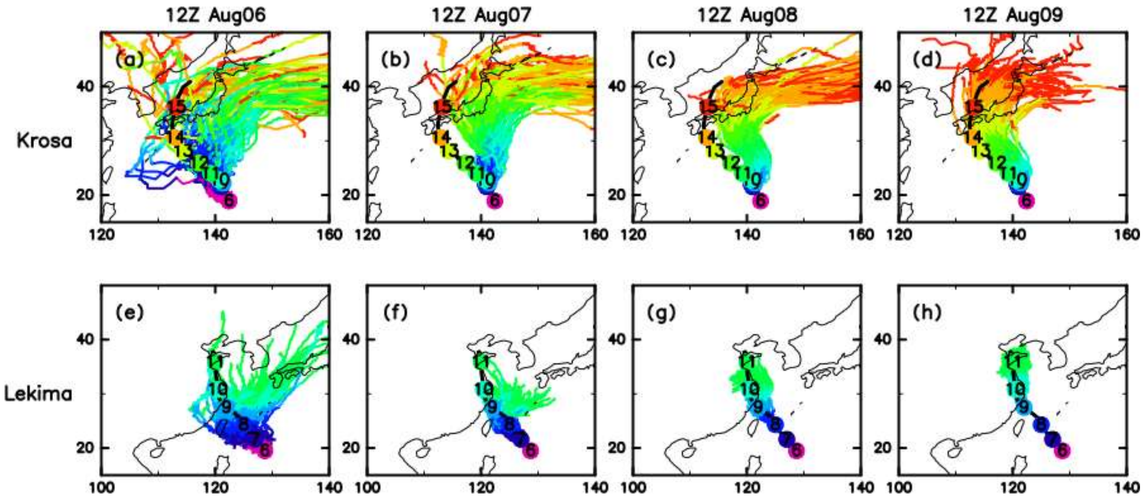

Fig. 2 Track forest for Krosa (a–d) and Lekima (e–h) by NICAM, initialized at 12:00 UTC, August 6th (a, e); 12:00 UTC, August 7th (b, f); 12:00 UTC, August 8th (c, g); and 12:00 UTC, August 9th (d, h), respectively.

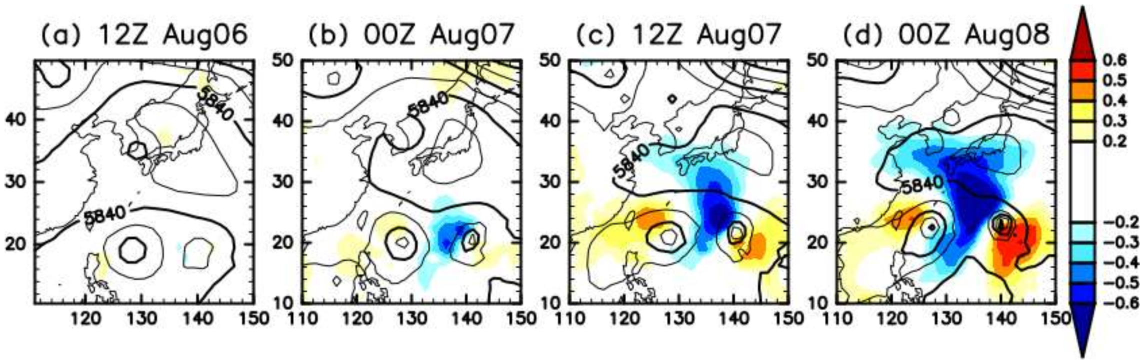

Fig. 3 Ensemble lag correlation between the 500-hPa geopotential height for 12:00 UTC, August 6th (a); 00:00 UTC, August 7th (b); 12:00 UTC, August 6th (c); and 00:00 UTC, August 7th (d) and Krosa's track forecast error at 12:00 UTC, August 11th.

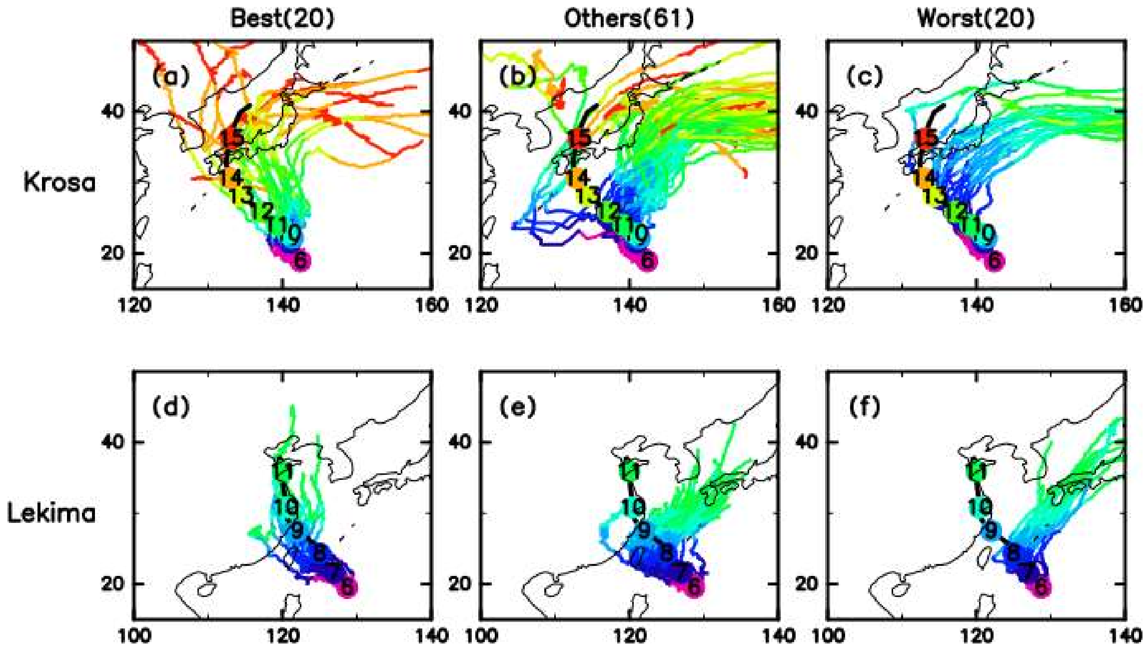

Fig. 4 Clustered track forecast for Krosa (a–c) and Lekima (d–f), initialized at 12:00 UTC, August 6th by the track forecast error for Krosa at 12:00 UTC, August 11th. Best 20 members (a and d), worst 20 members (c and f), and the remaining members (b and e).

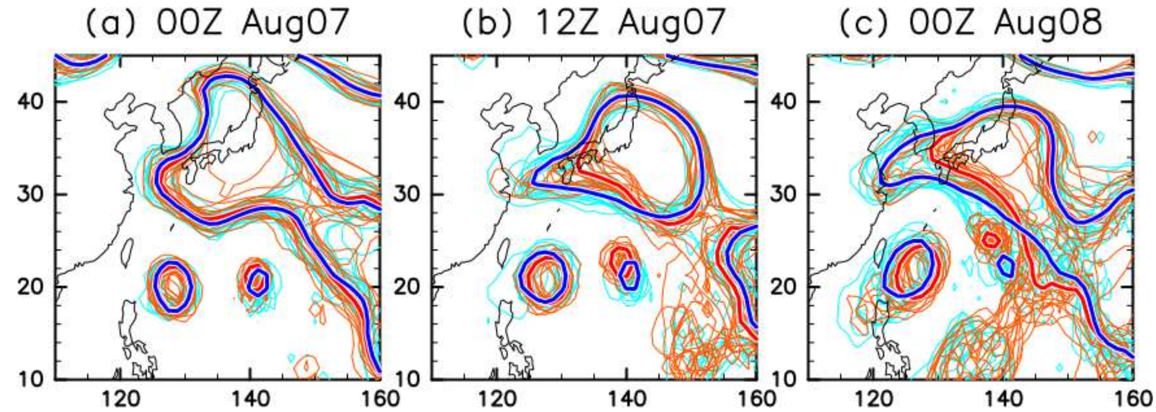

Fig. 5 Spaghetti diagram of the 500-hPa geopotential height valid for (a) 00:00 UTC, August 7th; (b) 12:00 UTC, August 7th; and (c) 00:00 UTC, August 8th. The orange (aqua) contours are forecasted by the worst (best) 20 members, and the thick lines are ensemble means of the best and worst members. The contours for 5760 and 5860 m are shown.

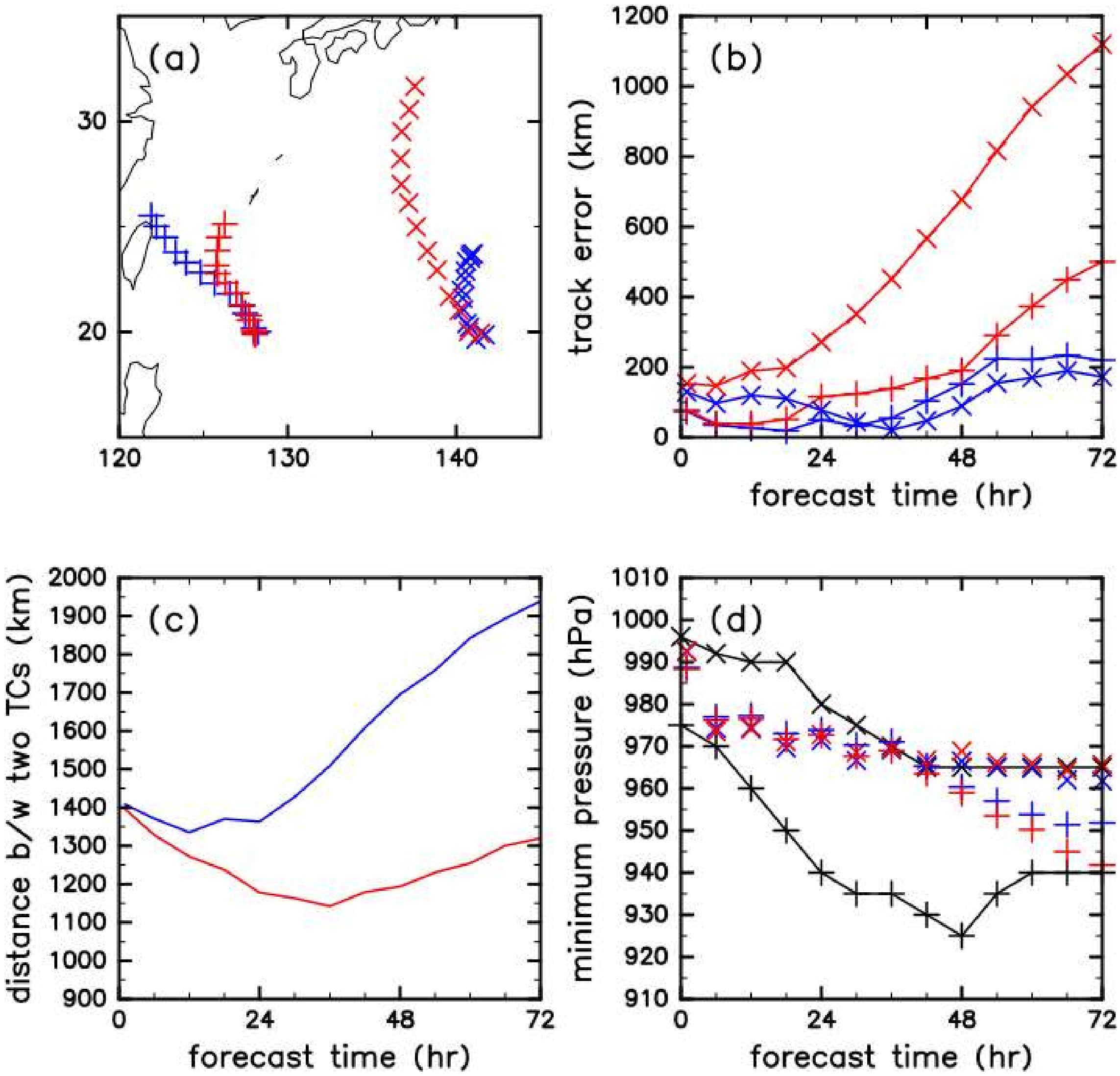

Fig. 6 Ensemble means of the best (blue) and worst members (red). (a) Track forecast, (b) track forecast error, (c) distance between Lekima and Krosa, and (d) central sea level pressure. The plus (+) symbol is for Lekima, and the cross (x) symbol is for Krosa.

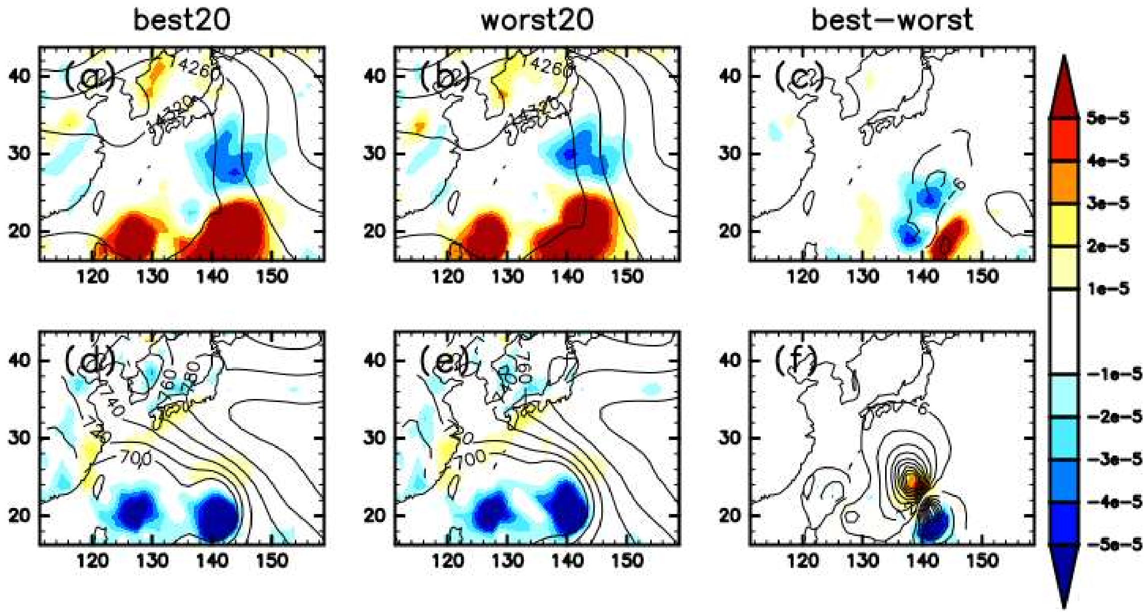

Fig. 7 Composite of the geopotential height and the divergences at 150 hPa (a–b) and 925 hPa (d–e), simulated for the best (a, d) and worst (b, e) 20 members and their differences (c, f).

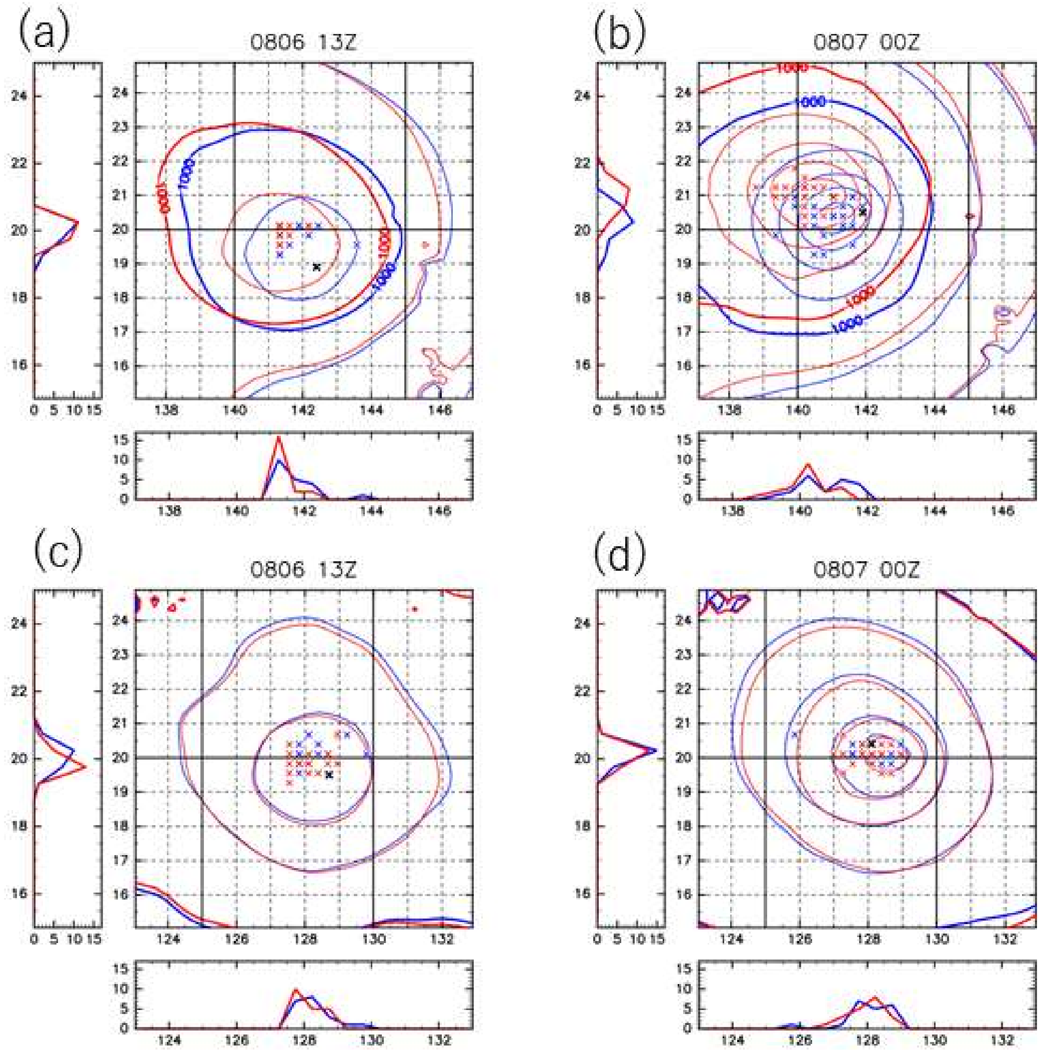

Fig. 8 Distributions of the TC center position and sea level pressure at FT = 1 (a, c) and FT = 12 (b, d) for Krosa (a–b) and Lekima (c–d).

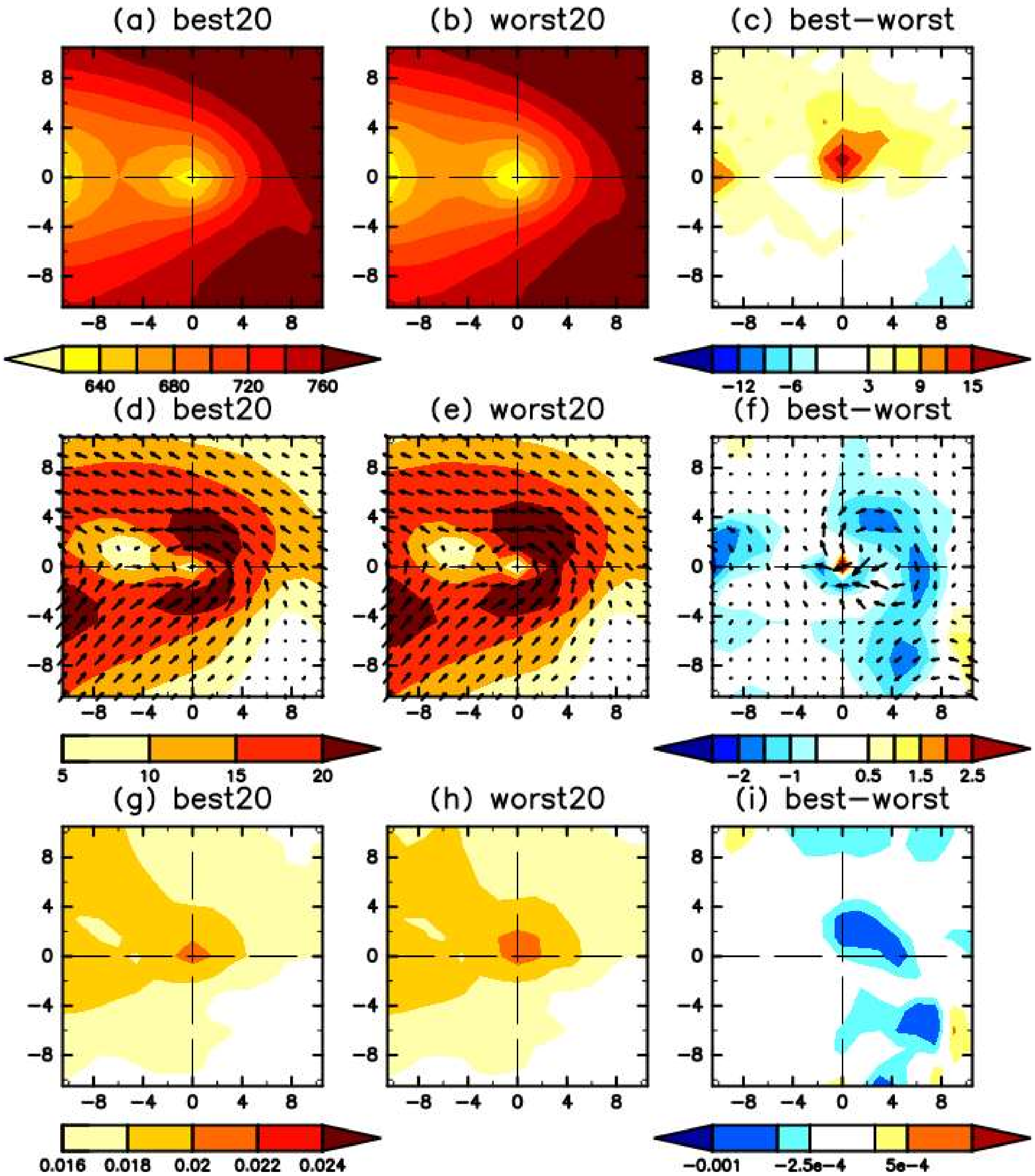

Fig. 9 Ensemble means of (a-b) SLP, (d-e) 10-m wind, and (g-h) specific humidity at 925 hPa, analyzed for the best (a,d,g) and worst (b, e, h) 20 members at 12:00 UTC, August 6th and their differences (c, f, i) around Krosa.

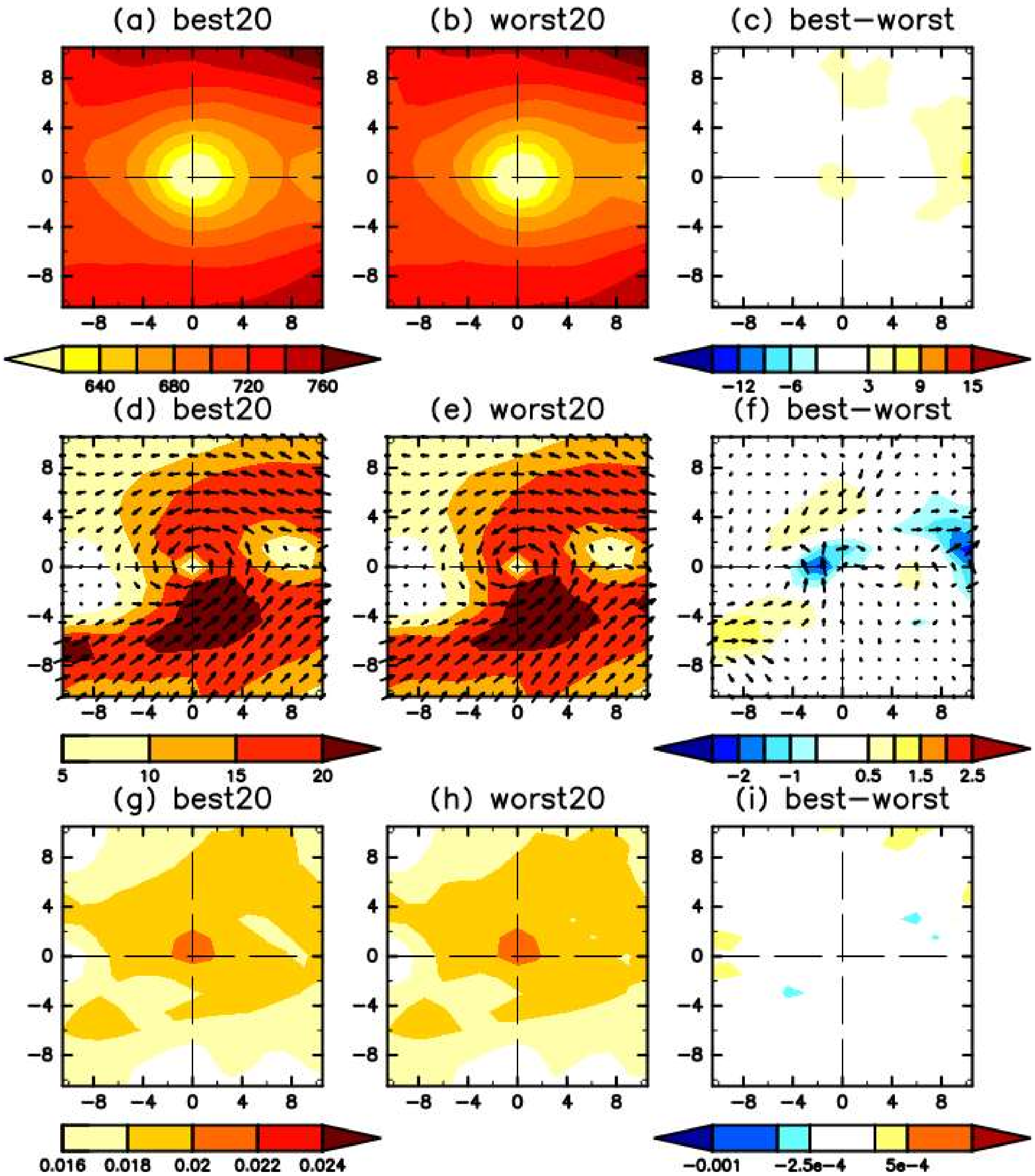

Fig. 10 Same as Fig. 9 but for around Lekima.

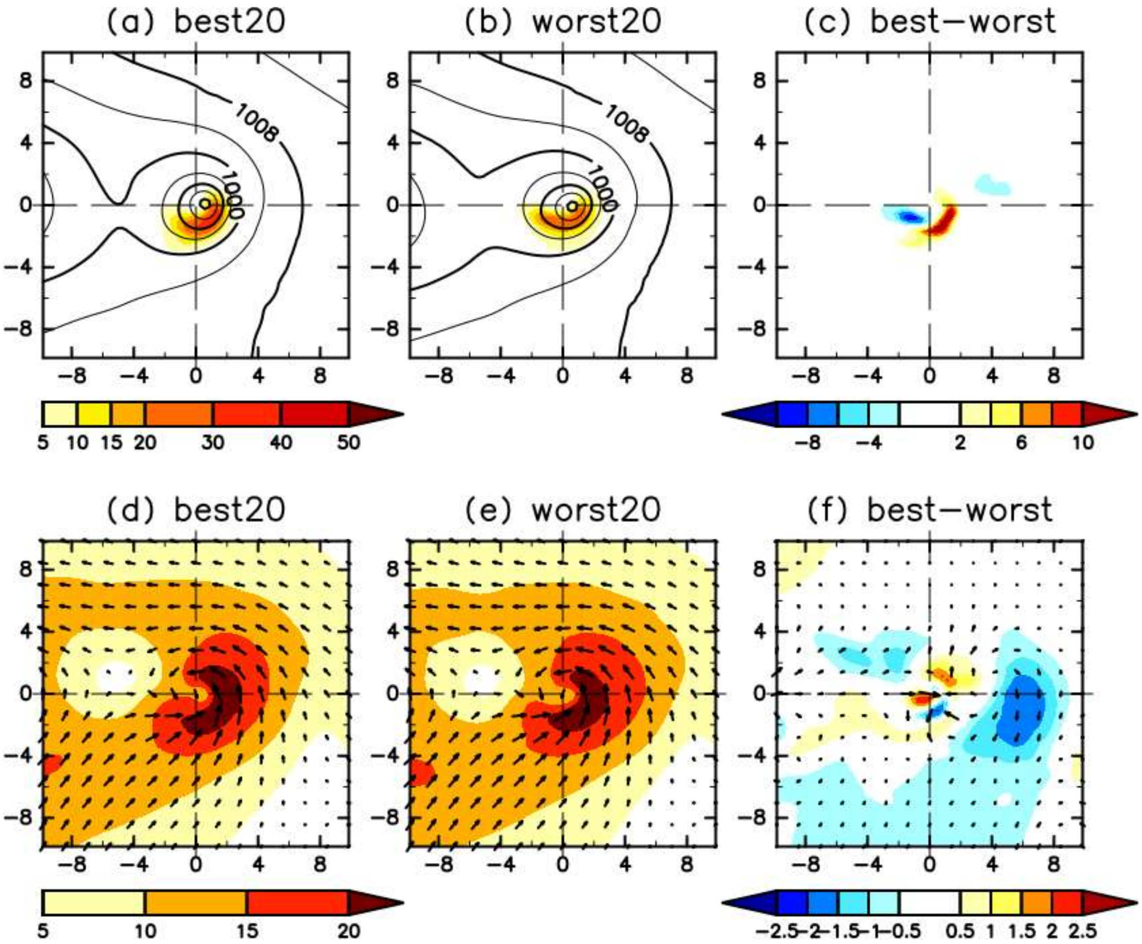

Fig. 11 TC relative composite of (a-b) SLP and precipitation and (d-e) 10-m wind during FT = 1–12 hours simulated for the best (a, d) and worst (b, e) members and their differences (c, f).

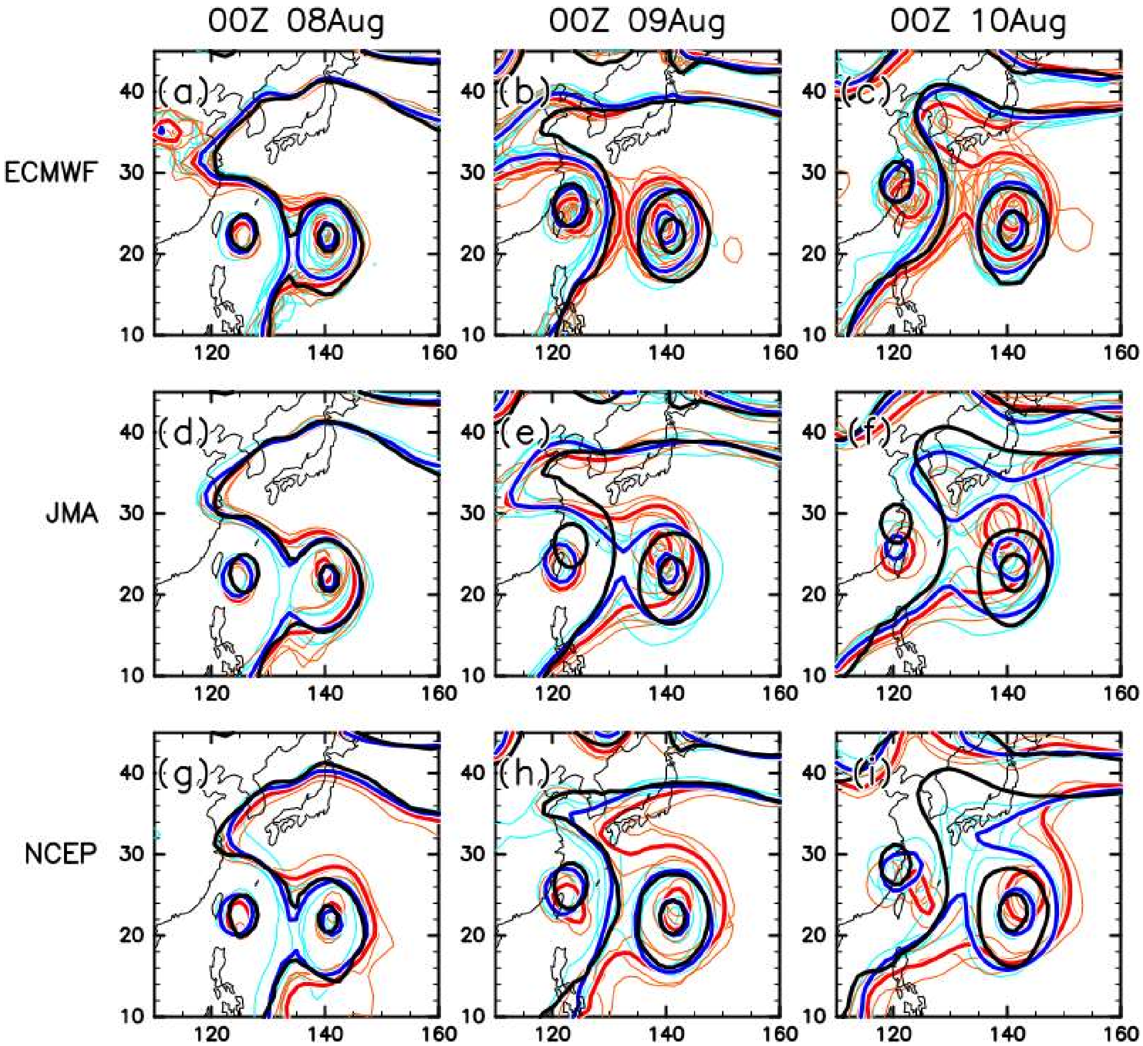

Fig. 12 Spaghetti diagram of the 500-hPa geopotential height valid for (a, d, g) 00:00 UTC, August 8th; (b, e, h) 00:00 UTC, August 9th; and (c, f, i) 00:00 UTC, August 10th by the ECMWF (a-c), JMA (d-f), and NCEP (g-i) models, initialized at 12:00 UTC, August 6th. The thin orange (aqua) contours were forecasted by the worst (best) 20% (10 for ECMWF, 5 for JMA, 4 for NCEP) of the members in terms of the Krosa track forecast error at 12:00 UTC, August 11th. The thick lines are ensemble means of the best and worst members, respectively. The black contours show the analysis by each model. The contours for 5760 and 5860 m are shown.

List of Tables

Table 1 Specifications of the operational ensemble prediction data archived at TIGGE as of August 2019.

	ECMWF	JMA	NCEP
Model resolution	Tco639 (Tco319 after 10 day)	TL479	TL574(TL190 after 8 days)
Archived data resolution	Same as model resolution	1.25 deg × 1.25 deg	1.0 deg × 1.0 deg
Perturbation method	Singular Vectors +Simplified Extended Kalman Filter	Singular Vectors + Local Ensemble. Transform Kalman Filter	Ensemble Kalman Filter
# of members	51	27	21